Activation-pathway transitions in human voltage-gated proton channels revealed by a non-canonical fluorescent amino acid.

Esteban Suárez-Delgado[1,2], M. E. Orozco-Contreras[1], Gisela E. Rangel-Yescas[1] and León D. Islas[1*]

From:

[1]Department of Physiology, School of Medicine, UNAM, Mexico City,04510, Mexico

[2]Current affiliation: Department of Biology, Xenon Pharmaceuticals Inc., 3650 Gilmore Way, Burnaby, BC V5G 4W8, Canada

*Correspondence to:

León D. Islas

Department of Physiology

School of Medicine

Universidad Nacional Autónoma de México (UNAM)

Circuito Escolar S/N, Ciudad Universitaria

Ciudad de México, 04510, México

leon.islas@gmail.com

ORCIDs

E. Suárez-Delgado: https://orcid.org/0000-0003-0147-3451

M.E. Orozco-Contreras: https://orcid.org/0000-0003-3315-4308

G. Rangel-Yescas: https://orcid.org/0000-0003-2766-6040

L.D. Islas: https://orcid.org/0000-0002-7461-5214

Significance statement

The activation mechanisms of voltage-gated proton channels (H_V1) are not well understood. Here we have combined patch-clamp fluorometry and a fluorescent non-canonical amino acid to uncover transitions in the activation pathway of human H_V1 that are modulated by voltage and the pH gradient.

Abstract

Voltage-dependent gating of the voltage-gated proton channels (H_V1) remains poorly understood, partly because of the difficulty of obtaining direct measurements of voltage sensor movement in the form of gating currents. To circumvent this problem, we have implemented patch-clamp fluorometry in combination with the incorporation of the fluorescent non-canonical amino acid Anap to monitor channel opening and movement of the S4 segment. Simultaneous recording of currents and fluorescence signals allows for direct correlation of these parameters and investigation of their dependence on voltage and the pH gradient (ΔpH). We present data that indicate that Anap incorporated in the S4 helix is quenched by an aromatic residue located in the S2 helix, and that motion of the S4 relative to this quencher is responsible for fluorescence increases upon depolarization. The kinetics of the fluorescence signal reveals the existence of a very slow transition in the deactivation pathway, which seems to be singularly regulated by ΔpH. Our experiments also suggest that the voltage sensor can move after channel opening and that the absolute value of the pH can influence the channel opening step. These results shed light on the complexities of voltage-dependent opening of human H_V1 channels.

Introduction

Voltage-gated, proton-permeable ion currents in a large variety of cell types and organisms are produced by the H_V1 gene (HVCN1 in humans), which encodes a membrane protein that is a member of the superfamily of voltage-sensing domains (VSDs) (Sasaki et al., 2006; Ramsey et al., 2006). These VSDs are also encountered in voltage-sensitive phosphatases (VSP) and voltage-gated ion channels (VGIC), and their principal function is to detect the

membrane potential difference and translate it into a conformational change that activates VSP and opens VGIC (Catacuzzeno and Franciolini, 2022).

H_V1 is thought to form ion channels activated by voltage and employing a mechanism of activation similar to the VSDs of canonical voltage-gated potassium, sodium and calcium channels (Gonzalez et al., 2012). The functions of H_V1 channels are diverse, including intracellular pH regulation (Ma et al., 2022), charge compensation during immune response (Ramsey et al., 2009), modulation of flagellar beating in spermatozoa (Lishko and Kirichok, 2010), bioluminescence (Eckert and Sibaoka, 1968), and possible roles in calcification processes in marine organisms (Taylor et al., 2011; Rangel-Yescas et al., 2021). Also, H_V1 is involved in different pathologies such as B cell malignancy (Hondares et al., 2014), breast cancer (Wang et al., 2012), and post-ischemic brain injury (Wu, 2014; Yu et al., 2020); consequently, in recent years H_V1 has emerged as a possible pharmacological target (Zhao et al., 2018; Zhang et al., 2022).

Among all voltage-gated proton channels sequenced, the human orthologue, hH_V1, is the most widely studied (Musset et al., 2008). This channel is thought to be a functional dimer formed by two subunits comprising an intracellular N-terminus, a bundle of four transmembrane helices (TMH, S1-S4) in the VSD fold, and a long intracellular alpha helix that mediates a coiled-coil interaction, mainly responsible for dimerization and cooperative activation (Koch et al., 2008; Lee et al., 2008; Tombola et al., 2008). The fourth alpha helix, S4, contains positive charges represented by three arginine residues (R205, R208, and R211) in the characteristic VSD repeats. S4 is thought to undergo an outward displacement and rotation in response to depolarization, mostly in accordance to the helical screw rotation and displacement model of voltage-gating (Li et al., 2015). Unlike canonical VGIC, H_V1 lacks the two TMH that make up the pore region in canonical ion channels (S5 and S6); therefore, the VSD of H_V1 has a double function: it is responsible for detecting the electrical potential across the membrane and forming the pathway through which the protons will move once the channel is activated.

A characteristic of H_V1 activation is its dependence on the pH gradient or ΔpH (pH_o - pH_i). Native proton channels were first shown to open at more negative voltages when the proton gradient points in the outward direction (Cherny et al., 1995). It was shown that for every unit of ΔpH, the voltage of mid activation shifts ~40 mV. Subsequently, all native and

95 cloned proton channels have been found to approximately follow this rule (Sasaki et al.,
96 2006; Ramsey et al., 2006; Rangel-Yescas et al., 2021; Musset et al., 2008; Smith et al., 2011;
97 Zhao and Tombola, 2021). Recent experiments suggest that the proton gradient produces
98 this effect by acting on the voltage sensor and not only affecting a close-to-open transition,
99 since gating currents and channel opening are similarly modulated (Schladt and Berger,
100 2020; Carmona et al., 2021). However, the molecular mechanisms through which protons
101 modulate voltage-sensor function are not known. Due to technical difficulties, such as not
102 having a pore structure separate from VSD or the impossibility of patch-clamping without
103 protons in the experiments, gating current recordings of H_V1 channels have been obtained
104 from mutants of the *Ciona* H_V1 (ciH_V1) orthologue (Carmona et al., 2018, 2021) or mutants
105 of human H_V1 (De La Rosa and Ramsey, 2018).
106 Patch-clamp Fluorometry (PCF) has been used to overcome these difficulties as a powerful
107 tool that allows investigation of electrically silent conformational changes in VSDs
108 associated with channel gating (Kusch and Zifarelli, 2014a), through following fluorescence
109 intensity changes of a dye that generally is attached to the channel protein via chemical
110 modification of cysteine residues or a fluorescent protein genetically encoded (Kusch and
111 Zifarelli, 2014b). In ciH_V1 and hHv1 proton channels, this technique has been employed to
112 obtain evidence of cooperative gating, S1 movement during activation, and the pH
113 sensitivity of S4 movement (Mony et al., 2015; Schladt and Berger, 2020; Qiu et al., 2013).
114 As in other voltage-gated channels, these studies made use of the fluorophore
115 tetramethylrhodamine (TMR), which was tethered to the S3-S4 linker, an extracellular-
116 facing part of the channel (Cowgill and Chanda, 2019). While fluorophores like TMR have
117 provided a means to observe conformational changes in many voltage-gated ion channels,
118 including Hv1, due to their large size and cysteine reactive nature, they are difficult to
119 incorporate in membrane-embedded portions of channels, without possible large
120 perturbation of the protein fold or result in unspecific incorporation. For these reasons,
121 incorporating a small fluorophore in the middle of transmembrane helices would be
122 advantageous. Here, we exploit the small size, comparable to aromatic amino acids, of a
123 genetically encoded fluorescent non-canonical amino acid, Anap (Chatterjee et al., 2013).
124 By incorporating Anap at various positions in the S4 segment, we assess the

125 conformational changes of the human voltage-gated proton channel (hHv1) in response to
126 voltage activation and pH modulation by performing patch-clamp fluorometry (PCF).
127 We find our measurements can resolve a transition during the deactivation process that is
128 strongly modulated by pH. Furthermore, we find that the changes in Anap fluorescence
129 could be partially due to interaction with aromatic amino acids within H_V1.
130
131 **Results**
132 ***Incorporation of Anap into hH_V1***
133 To study voltage-dependent transitions in a voltage sensor using patch-clamp fluorometry,
134 it is desirable that the introduced fluorescent probe does not produce a major structural
135 perturbation of the target protein. The relatively recently developed probe Anap (3-(6-
136 acetylnaphtalen-2-ylamino)-2-aminopropanoic acid) is a small non-canonical fluorescent
137 amino acid (Figure 1B), which has been shown to be easily genetically-encoded in proteins
138 expressed in eukaryotic cells (Chatterjee et al., 2013; Puljung, 2021) Moreover, Anap has
139 been successfully used as a reporter of voltage-dependent conformational changes
140 (Kalstrup and Blunck, 2013) and as a FRET pair (Gordon et al., 2018) to probe ion channel
141 dynamics. In this study, Anap was inserted into specific positions of the S4 segment of the
142 human H_V1 proton channel (hH_V1) sequence (Figure 1A), with the purpose of examining its
143 voltage and pH-dependent dynamics.
144 We selected the S4 helix as insertion target, since this region of the channel is proposed to
145 undergo a voltage-dependent outward displacement that has been previously studied with
146 different approaches, including voltage-clamp fluorometry (13–15).
147 We were able to successfully substitute amino acids by Anap at positions Q191 in the S3-S4
148 linker and A197, L198, G199, L200, L201, and I202 in the S4. Anap efficiently rescued
149 expression of channels containing an amber stop codon (TAG) in the selected position, as
150 judged both by appearance of red fluorescence produced by the mCherry fluorescent
151 protein appended in the C-terminus (Figure 1C and Figure 1-supplement 1A) or the
152 appearance of proton currents recorded from HEK 293 cells in the whole-cell patch-clamp
153 configuration (Figure 1D, Figure 1-Supplement 2 and Supplementary Table I).
154 The substituted channels gave rise to voltage-activated currents, with similar range of
155 activation to WT as judged by their conductance vs. voltage (G-V) curves (except I202Anap

156 channels). Furthermore, that Anap was able to specifically rescue TAG-containing channels
157 was demonstrated by control experiments in cells cotransfected with mutant channels and
158 the pANAP plasmid in the absence of Anap, which showed absence or very small proton
159 currents as compared to cells cultured in the presence of Anap (Figure 1-supplement
160 1B).The observed fluorescence emission spectrum of the Anap signal present in the
161 membrane (Figure 1C), which presumably originates mostly from Anap incorporated into
162 channels, shows that there are no major or systematic variations on the peak emission
163 wavelength (Figure 1E). The peak emission wavelength for all positions varies, but is near
164 485 nm, except the most C-terminal and presumably deepest position, I202Anap, which is
165 477 nm (Figure 1-Supplement 3A). This result suggests that the local environment of Anap
166 in these positions, except 202Anap, is very similar and consistent with a mostly polar
167 environment since the peak emission of Anap in aqueous solution is ~486 nm.
168 Figure 1E also shows that the emission spectra of positions other than Q191Anap exhibit a
169 small extra peak near 610 nm, that corresponds to the peak emission of mCherry. Since the
170 excitation peak of mCherry is 587 nm (Shaner et al., 2004) , we performed experiments
171 with hH_V1-mCherry channels to measure direct mCherry excitation by our 405 nm laser.
172 The results indicate that this peak is mostly produced by direct excitation of mCherry at
173 405 nm (Figure 1-Supplement 3B).
174
175 ***Insensitivity of Anap to pH***
176 In order to use Anap as a reporter of conformational changes in H_V1 proton channels, and
177 given that these channels are able to change the pH of the surrounding solution (De-la-Rosa
178 et al., 2016; Zhang et al., 2016), we first wanted to validate if this fluorophore is insensitive
179 to pH changes. The amino acid form of Anap that we use is the methyl-ester, which contains
180 amino and carboxy groups. The fluorescence of methyl-ester Anap could be affected by
181 protonation because it could alter electron distribution, for this reason, we reasoned that
182 the best assay to test the pH dependence of Anap fluorescence is to use already
183 incorporated Anap. For this purpose, we used the mutant Q191Anap, which incorporates
184 Anap in the S3-S4 loop, which faces the extracellular solution, even in the deactivated state
185 of the channel (Figure 1A). Since the emission spectrum of Q191Anap channels was
186 measured from non-voltage clamped transfected HEK cells, fluorescence was obtained only

187 from membrane regions to assure that the signal comes mostly from channels exposed to
188 the extracellular solution changes and not channels in intracellular compartments, which
189 will not be exposed to the pH changes.
190 To ensure that most of the fluorescence is collected from channels in the membrane, the
191 membrane region was identified by the fluorescence of mCherry-containing channels that
192 clearly delineates it (Figure 2-Supplement 1). Spectra were then collected only from this
193 small region of membrane.
194 These measurements showed that the fluorescence of channel-incorporated Anap is not
195 significantly changed in intensity or shape of the emission spectrum over the pH range 3 to
196 9 (Figure 2A and B), indicating that this fluorophore is insensitive to pH and that Anap
197 fluorescence should not be affected by local pH changes, which might be produced as a
198 consequence of proton currents.
199 As a further test of our data showing pH-insensitivity of channel-incorporated Anap and to
200 validate the use of Anap in proton channels, we incorporated the amino acid in a position at
201 the N-terminus of the channel, V62Anap. This amino acid is located in the intracellular part
202 of the channel and should be subject to changes in local internal pH during channel
203 activation (De-la-Rosa et al., 2016) but not show changes in fluorescence as a function of
204 voltage-dependent conformational changes. As expected, we did not detect Anap
205 fluorescence changes, although the amino acid was incorporated into functional channels,
206 as judged from proton currents recorded simultaneously with fluorescence (Figure 2C and
207 D). This result further supports the use of Anap in voltage-gated proton channels to
208 measure conformational changes.
209
210 ***Voltage-dependent changes of Anap fluorescence***
211 Previous experiments in which other dyes like tetra-methyl-rhodamine maleimide (TMRM)
212 were used to label cysteine residues located in the amino-end of the S4 segment of voltage-
213 sensing domains, including the *Ciona* and human H_V1 channels (Schladt and Berger, 2020;
214 Mony et al., 2015; Qiu et al., 2013), usually result in fluorescence signals that are reduced
215 upon depolarization by a voltage-dependent quenching process (Vaid et al., 2008; Cha and
216 Bezanilla, 1998). In contrast, when we incorporate Anap at position A197, located towards
217 the extracellular end of the S4, depolarization induced an increase of the fluorescence,

218 along with proton currents. The fluorescence increase saturates at depolarized voltages,
219 suggesting that it is produced by a saturable process such as voltage-sensor activation. The
220 direction of this fluorescence change is the same when measured at a ΔpH of 0 or 2,
221 suggesting the same conformational change in the S4 voltage sensor occurs at different pH
222 gradients, albeit over a different range of voltages (Figure 3A and B).
223 We compared the kinetics of current and fluorescence by fitting an exponential function to
224 the second half of the signal time course and plotted the time constant as a function of
225 voltage (Figure 3C). Both current and fluorescence have the same voltage dependence, but
226 the current is ~1.3 times faster than the fluorescence. Although not a very large difference,
227 this can be explained by an overestimation of the current time course due to slight proton
228 depletion observed with large currents.
229 When F-V and G-V curves are plotted together, it is evident that sensor movement
230 paralleled the activation of the proton conductance. At three different values of the pH
231 gradient (ΔpH 0, 1 and 2), both the F-V and G-V curves are almost superimposable and shift
232 along the voltage axis by the same amount of ~40 mV/pH unit (Figure 3D), which is
233 expected of H_V1 channels (Cherny et al., 1995). Only at ΔpH = 2 the fluorescence signal is
234 shifted to slightly more negative voltages than the conductance and only at voltages at
235 which channel activation begins. The observed voltage shift of the G-V is ~31 mV from ΔpH
236 2 to 1 and ~43 mV from ΔpH 1 to 0 and is very similar for the F-V curves. This result
237 indicates that the ΔpH-dependence of gating is preserved in channels with incorporated
238 Anap, and that the voltage sensor movement occurs in the same voltage range as the
239 formation of the proton permeation pathway.
240 Anap is an environmentally sensitive dye, which shifts its emission to red wavelengths in
241 increasingly polar solvents (Figure 3-Supplement 1). To understand the origin of the
242 increased fluorescence observed during activation, we measured the emission spectra of
243 A197Anap in voltage-clamped cells at different voltages. Fluorescence was measured from
244 channels in the membrane region, which are identified by the mCherry signal, similar to
245 Figure 1C. Figure 3E plots the spectra obtained at voltages ranging from -100 to 140 mV
246 and it shows that the fluorescence increases with depolarization and has the same voltage-
247 dependence as the fluorescence measured in Figure 3A, B and C at the same ΔpH (Figure

248 3E, inset). On the other hand, the peak emission wavelength remains the same at negative
249 or positive voltages, indicating that the increase in fluorescence is not due to
250 depolarization-driven wavelength shifts of the emission spectra. We interpret this result as
251 an indication that Anap incorporated at position A197 remains in a polar environment at
252 all voltages or that small changes in polarity change the quantum yield of Anap but not the
253 emission spectrum.
254
255 ***H_V1-197Anap is quenched by a phenylalanine in the S2***
256 The increase of the Anap fluorescence at position 197 in the S4 seen with depolarization
257 could be interpreted as a reflection of an outward movement of the S4 and exposure of
258 Anap to a more polar environment (Figure 3 -Supplement 1), that in principle will produce
259 a red shift of the emission spectrum and an increase of the fluorescence that is detected.
260 However, as shown in Figure 3E, the shape of emission spectrum of Anap remains
261 unchanged at all voltages and with a constant emission peak at ~480 nm, indicating that
262 the fluorophore remains in a polar environment in the closed and open states and thus, a
263 change in local polarity is likely not the principal cause of dequenching.
264 Many fluorophores can be quenched by aromatic amino acids through mechanisms such as
265 π-stacking or photoinduced electron transfer, both mechanisms require close proximity
266 (Islas and Zagotta, 2006; Klymchenko, 2017; Pantazis and Olcese, 2012; Young and Artigas,
267 2021). Evidence for the existence of a quenching group near Anap incorporated in the S4
268 can be obtained from examination of the ratio of fluorescence of Anap and mCherry in
269 channels as a function of its position along the S4 (Figure 4-Supplement 1). This analysis
270 shows that for positions deeper into the S4 segment, the Anap/mCherry ratio diminishes,
271 suggesting that in those sites Anap is closer to a quenching group.
272 For these reasons, it is conceivable that the Anap quencher in H_V1, could be an aromatic
273 residue located near the introduced fluorophore in the closed state and upon S4 movement,
274 increases its distance, generating the observed dequenching. We used a structural model of
275 H_V1 derived from experimental data (Randolph et al., 2016) and replaced A197 with Anap.
276 Figure 4A shows Anap in salmon-colored spheres and highlights aromatic residues within
277 the transmembrane domains of a monomer as dotted spheres. A possible candidate for an

278 Anap quencher is F150 (yellow spheres), because this residue is the closest aromatic to
279 Anap that is not in the S4 and F150 will presumably remain in its position as 197Anap
280 undergoes an outward displacement with depolarization. In contrast, other aromatic
281 residues which are closer to 197Anap and are part of the S4, will presumably move with all
282 the S4 as a rigid body. Incidentally, an equivalent phenylalanine to F150 has been identified
283 as the charge transfer center in canonical voltage-gated potassium channels and in H_V1
284 (Tao et al., 2010; Hong et al., 2013).
285 To test this hypothesis, we made the double mutant F150A-A197Anap and estimated the
286 relative amount of basal Anap quenching, by comparing the emission spectra of both Anap
287 and mCherry in the same membrane region. Figures 4B and C shows that the double
288 mutant displays a significantly increased Anap fluorescence (~60 %) relative to mCherry,
289 when compared to A197Anap alone, suggesting that indeed, phenylalanine 150 is capable
290 of quenching Anap in the closed state (at the resting potential of HEK cells of -20 to -40 mV
291 (Thomas and Smart, 2005b) and at the employed $\Delta pH \sim -0.2$ ($pH_o = 7$) most channels
292 should be in the closed state).
293 Despite having removed the quenching group, F150A-A197Anap channels still show
294 voltage-dependent fluorescence changes (Figure 4D), suggesting the presence of additional
295 quenchers or that in the absence of F150, Anap at 197 becomes sensitive to polarity
296 changes.
297 The voltage dependence of the fluorescence signals from F150A-A197Anap channels shows
298 significant differences from those of A197Anap alone (Figure 4E). At values of ΔpH of 0 and
299 1, fluorescence precedes the increase in conductance, indicating that the conformational
300 change of the S4 segment occurs at more negative voltages than the formation of the
301 proton-permeable pathway. This effect is more pronounced at ΔpH = 1. Interestingly, the
302 difference of $V_{0.5}$ of the F-V curve between ΔpH= 0 and 1 is ~58 mV, similar for A197Anap,
303 which is ~46 mV.
304
305 ***A distinct gating transition detected by Anap fluorescence***
306 The fluorescence time course of the F150A-A197Anap channels shows an interesting
307 characteristic; the OFF signals (F_{off}) that are produced at the return of the voltage to the

holding potential and represent the return of the voltage sensor to the resting states, show a two-component kinetic behavior. This is particularly evident at ΔpH = 0 (Figure 4D), where F_{off} shows a very rapid quenching followed by a much slower component, suggesting that the voltage sensor can move back to its resting position at varying rates.

To explore the kinetics of fluorescence signals during repolarization, and since this double mutant removes a quenching group, we used the hH_V1-201Anap channels. We reasoned that this mutant channel, which has Anap in a deeper position in the S4 and presumably closer to F150 in the closed state, might be a better reporter of the kinetics of S4 movement.

Figures 5A, B and C show simultaneous current and fluorescence recordings from hH_V1-L201Anap channels at three different ΔpH values of 0, 1 and 2. As with the hH_V1-A197Anap construct, the voltage-dependence of the conductance and fluorescence are almost superimposable and shows a large shift of >40 mV/pH unit (Figure 5D).

The most remarkable feature of these fluorescence traces is that, at ΔpH = 0, the OFF signal during repolarization (F_{off}) has two distinct kinetic components. The deactivation tail currents at -60 mV decay exponentially, with a time constant of 141 ± 55 ms, while the F_{off} can be fit to a sum of two exponentials with time constants of 129 ± 68 ms and 8.6 ± 0.74 s. (Figure 5-Supplement 1). The presence of the two components in F_{off} suggest that the return of the voltage sensor to its resting state can occur at varying rates. In particular, the slow component is consistent with the immobilization of the off-gating charge observed in monomeric *Ciona* H_V1 channels (Carmona et al., 2018). The slow off-component is also present at ΔpH = 1 and 2, although its amplitude is smaller. We did not undertake a systematic kinetic analysis of current and fluorescence traces during channel activation due to the alterations that proton depletion cause on the current time course, especially for the larger currents observed at ΔpH = 2.

Instead, to qualitatively understand the kinetics of the fluorescence signals, we used a simplified kinetic model of channel activation (Scheme I), similar to a model that was previously used to study the voltage-dependent kinetics of hH_V1 (Villalba-Galea, 2014).

$$C_0 \underset{k_{10}}{\overset{k_{01}}{\rightleftharpoons}} C_1 \underset{k_{21}}{\overset{k_{12}}{\rightleftharpoons}} C_2 \underset{k_{32}}{\overset{k_{23}}{\rightleftharpoons}} O_3$$

Scheme I

In this model, one of the backward transitions (k_{21}) between closed states is set to be much slower than the open to closed transition (O_3->C_2), resulting in a large difference between the closing kinetics of the ionic current, mostly determined by k_{32}, and the fluorescence signals. This kinetic difference can account for the biphasic behavior of the F_{off} signal, and especially the slow component of its time course (Figure 5E). The model also indicates that when the internal pH is lower than the external pH (ΔpH=2), this slow rate constant is more affected than any other, indicating a conformational step that is especially sensitive to pH.

While the simple model in Scheme I can account qualitatively for the observed kinetics of 201Anap channels, the experimental F-V relationship is superimposable on the G-V curve (ΔpH=0 and 1) or positively shifted by ~10 mV (ΔpH=2) with respect to the G-V curve, which is not a feature predicted by Scheme I and is reminiscent of channels that can open to multiple open states, without the need of full voltage sensor activation (Stefani et al., 1997). This observation suggests that hH_V1 channels operate via a more complicated mechanism that the sequential gating illustrated by Scheme I, which might include channel opening before complete voltage-sensor movement. We tested a simple version of such an allosteric model and show that it can account, at least qualitatively, for current and fluorescence kinetics and for the relationships between G-V and F-V curves at varying ΔpH (Figure 5-Supplement 2). Interestingly, in this model the slow deactivation rate constant is also the step with the most sensitivity to pH (Supplementary Table III).

Absolute pH values are determinants of voltage sensor movement.

One of the most intriguing characteristics of H_V1 channel gating, is its steep modulation by the pH gradient. While it has been shown that this modulation depends on the value of ΔpH, regardless of how it is set up (Cherny et al., 1995), there is evidence that the absolute value of pH can also exert an effect on gating (Cherny et al., 2015). In most of our experiments, the pH gradient was set up with a low value of intracellular pH, between 5.5

368 and 6.0. To test the effect of absolute pH, we carried out experiments with the same ΔpH of
369 0, with symmetric low (5.5/5.5) or high (7/7) intra/extracellular pH. The expectation was
370 that, if pH gating of hH_V1 depends only on the pH gradient, the voltage sensor should move
371 with essentially the same characteristics. Surprisingly, the fluorescence signals display
372 important differences, as do the proton currents. Our results in Figure 6 show that when
373 compared to ΔpH = 0 (5.5/5.5), the fluorescence in symmetric pH_o and pH_i = 7.0 has a rapid
374 return of the F_{off} signal (Figure 6A and B). Interestingly, the voltage dependence of the F-V
375 relationship is very similar for (5.5/5.5) or (7/7) conditions, while in (7/7) the proton
376 current appears at more negative voltages than the bulk of the fluorescence (Figure 6C).
377 These results suggest that the voltage range of movement of the voltage sensor, as reported
378 by the fluorescence of 201Anap, is dependent on the ΔpH, since the $V_{0.5}$ of the F-V is the
379 same in pH_o/pH_i =5.5/5.5, while the opening of the proton conduction pathway in pH_o/pH_i
380 =7/7, can occur after only a fraction of the voltage sensor movement has occurred and this
381 coupling between voltage sensing and channel opening can be increased by low pH.
382

383 **Discussion**

384 In the experiments described here we have implemented patch-clamp fluorometry in
385 combination with incorporation of a fluorescent non-canonical amino acid (NCAA) to study
386 voltage-dependent gating in hH_V1 proton channels. Although voltage-clamp fluorometry
387 (VCF) using TMRM has been used previously to study H_V1 channels (Qiu et al., 2013; Mony
388 et al., 2015; Schladt and Berger, 2020), employing the fluorescent Anap NCAA has the
389 advantages of being a smaller size probe and improving the specificity of fluorescence
390 signals, since it is genetically encoded. The small size of Anap allowed us to incorporate the
391 fluorophore into functional channels in several sites along the S4 and the S3-S4 loop. Since
392 Anap was developed as an environmental sensitive probe, the fact that the emission
393 spectrum of Anap in these sites is very similar to that of Anap in water, suggests that these
394 residues are solvated in the native H_V1. The only position that shows a blue-shifted Anap
395 spectrum is I202, which is the most C-terminal residue explored and might burry the Anap
396 R-group in a more hydrophobic environment.

397 Since the activity of H_V1 proton channels can change the local concentration of protons
398 near the conduction site and fluorescence probes have been used to detect these proton
399 fluxes (De-la-Rosa et al., 2016; Zhang et al., 2016), we addressed whether Anap could
400 change its fluorescence as a function of pH. We show that Anap is highly insensitive to pH
401 in the range 4 to 8 and it does not change fluorescence in conditions in which high outward
402 fluxes can change the local intracellular pH. Our experiments confirm that Anap can be
403 used without interference from local changes in proton concentration.
404 When incorporated at position 197, Anap produced fluorescence signals that indicate an
405 increase in intensity with depolarization and saturated in magnitude at positive potentials.
406 This behavior indicates dequenching of Anap as the S4 segments undergoes an outward
407 movement during the activation conformational change. Anap has been incorporated in
408 other membrane proteins, including the *Shaker* potassium channel, in which Anap was
409 incorporated in the S4-S5 linker and displayed fluorescence quenching upon depolarization
410 (Kalstrup and Blunck, 2018). Anap has been incorporated in the S4 of the
411 hyperpolarization-activated cyclic nucleotide-gated (HCN) channel (Dai et al., 2019), where
412 it is quenched or dequenched upon hyperpolarization in a position-dependent manner. It
413 has also recently been incorporated at the bottom of the S4 in the voltage-dependent
414 phosphatase, CiVSP (Mizutani et al., 2022), where it becomes quenched upon
415 depolarization. The direction of the fluorescence changes due to S4 motion are difficult to
416 predict, since, as we have shown, Anap's fluorescence can be affected by both the local
417 environment's polarity and interaction with specific quenching groups that are part of the
418 channel sequence.
419 The fluorescence changes we observe in 197Anap channels indicate that the G-V and F-V
420 relationships have almost the same voltage-dependence at the ΔpH values tested,
421 suggesting that S4 movement closely follows channel opening, and that S4 movement and
422 activation of the proton conductance are equally affected by the proton gradient. A similar
423 conclusion has been reached in studies measuring S4 movements of hH_V1 by fluorescence
424 (Schladt and Berger, 2020) or in *Ciona* H_V1 by gating current recordings (Carmona et al.,
425 2021). Interestingly, these changes in fluorescence as a function of voltage, are not
426 accompanied by changes in the emission spectrum of Anap, suggesting that the probe

427 remains in a solvated environment regardless of the state of the channel. This is in
428 accordance with the finding that the VSD that forms hH_V1 channels has a large extracellular
429 cavity able to contain many water molecules (Ramsey et al., 2010).
430 Since Anap remains solvated in the closed and open state, what is the origin of the reported
431 fluorescence changes? As is common with other fluorescent probes, we hypothesized that
432 an aromatic residue could act as an Anap quencher and thus found that an aromatic outside
433 the S4 close enough to have this function is F150. Mutation F150A in the 197Anap
434 background produced an increased Anap/mCherry fluorescence intensity as compared to
435 197Anap alone, indicating reduced quenching. This result suggests that 197Anap moves
436 away from F150 as the S4 segment moves outward during channel activation. It should be
437 noted that F150A-197Anap channels still produce fluorescence changes upon
438 depolarization. This suggests that other amino acid residues apart from F150 (aromatic,
439 charged) can also quench Anap or changes in Anap's quantum yield are still being produced
440 by voltage-dependent solvent accessibility.
441 F150 has been shown to be part of a "hydrophobic gasket" through which S4 charges slide
442 during channel activation. Mutations at this position and at W207 in the S4 produce altered
443 gating (Banh et al., 2019; Cherny et al., 2015; Wu et al., 2022). In our case, F150A-197Anap
444 shows a reduced shift of the G-V between ΔpH 0 and 1, from the expected ~40 mV to 22
445 mV, although the F-V curve shifts by 58 mV. These changes could be explained by altered
446 movement of S4 through F150A, leading to changes in the coupling between voltage sensor
447 movement and proton conductance activation. Also, this is the first time that F150 is
448 reported as a possible actor in the pH-sensing mechanism of H_V1.
449 Substitution of L201 for Anap allowed us to uncover a slow step in the deactivation
450 pathway. The fluorescence signal observed upon channel closure by repolarization at ΔpH
451 = 0 shows two components, one of which is much slower than channel closing as reported
452 by the tail current. The fact that tail current is faster than the slow component of the
453 deactivation fluorescence signal indicates that the latter is produced by a slow
454 intermediate transition. This experimental observation is recapitulated by a simple kinetic
455 model. Interestingly, recordings of gating currents in mutant *Ciona* H_V1 channels show that
456 the charge return after depolarization can be very slow, producing gating charge

457 immobilization (Carmona et al., 2018). This observation of a singular slow transition in
458 hH_V1 activation illustrates the value of fluorescence recording with a small probe such as
459 Anap.
460 Our data thus far indicates that a fraction of S4 movement, as reported by the F-V relation,
461 occurs before the increase of the proton conductance, and that S4 movement can continue
462 after channel activation. Comparison of the $V_{0.5}$ values of Q-V and G-V curves in hH_V1
463 channels (De La Rosa and Ramsey, 2018) indicates that charge moves at slightly more
464 negative values than conductance, but not at all ΔpH values. Fluorescence changes depend
465 on all the conformational states in which the fluorophore has distinct fluorescence values,
466 while gating currents are produced during transitions between conformations with state-
467 dependent charge distributions (Cha and Bezanilla, 1997). For these reasons, F-V and Q-V
468 curves of multistate channels are not expected to be identical or contain the same
469 information.
470 Our fluorescence data are consistent with recent experiments that have shown that the
471 characteristic gating effect of the proton gradient on voltage-gated proton channels comes
472 about by a conformational change that affects voltage sensor movement and not a channel
473 opening transition happening after voltage-sensor activation. Furthermore, our modeling
474 suggests that all transitions in the activation pathway, including a characteristic slow
475 transition detected by fluorescence are modulated by ΔpH.
476 The mechanism of ΔpH modulation is still unknown. It has been proposed that the energy
477 stored in the pH gradient is directly coupled to S4 movement to produce ΔpH-dependent
478 gating (Carmona et al., 2021). We have previously proposed an allosteric model in which
479 both extracellular and intracellular protons can affect local electrostatic networks and
480 bring about ΔpH-gating (Rangel-Yescas et al., 2021). This class of models predicts the
481 existence of multiple open states, which is supported by the observation that S4 movement
482 can happen after channel opening.
483 A mechanism in which the proton gradient energy is coupled to S4 movement predicts that
484 the absolute value of pH should not influence gating. Interestingly, we have observed that
485 the absolute pH values used to set up a ΔpH = 0 do affect gating. When pH_o=5.5/pH_i=5.5, G-
486 V and F-V are almost superimposed and the F_{off} signal has a fast and slow component; in

487 contrast, when pH_o=7/pH_i=7, the F-V curve has almost the same voltage-dependence, but
488 conductance can be observed at more negative voltages and the F_{off} signal only contains the
489 fast component. These results suggest that the absolute pH in the extracellular side of the
490 channel is a determinant of the steady-state gating, presumably modulating the slow rate
491 constant in the activation pathway.
492
493 **Materials and Methods**
494 *Molecular biology and HEK cell expression*
495 A plasmid containing the human voltage-gated proton channel (hH_V1) was a gift from Dr.
496 Ian Scott Ramsey (Virginia Commonwealth University, Richmond, VA). We used the
497 fluorescent protein mCherry as a reporter to verify L-Anap incorporation. The construct
498 hH_V1-mCherry was made by the PCR overlap technique, adding the sequence of fluorescent
499 protein mCherry after the C-terminus of hH_V1 with the following linker sequence: (Gly-Gly-
500 Ser)$_3$. This construct was subcloned into the pCDNA3.1 vector. For all hH_V1-TAG mutants,
501 an amber codon (TAG) was introduced using appropriate mutagenic oligonucleotides and a
502 protocol for whole plasmid site-directed mutagenesis employing KOD polymerase (Merck
503 Millipore, Germany) as detailed in manufacturer's instructions and previous work (Zheng
504 et al., 2004; Munteanu et al., 2012). The bacterial methylated DNA templates were digested
505 with the DpnI restriction enzyme, and the mutant plasmids were confirmed by automatic
506 sequencing at the Instituto de Fisiología Celular, UNAM.
507 We used HEK293 cells for channel expression and L-Anap incorporation experiments. The
508 HEK cells used in this study were found free of mycoplasma infection (Sigma-Aldrich
509 mycoplasma detection kit). These cells were cotransfected with 0.1 – 1 μg of mutant hH_V1-
510 TAG plasmid and 0.7 μg of pAnap plasmid (a gift from Dr. Sharona Gordon, University of
511 Washington, Seattle, WA) using the transfection reagent JetPei (Polyplus-transfection).
512 The pANAP plasmid contains the orthogonal pair tRNA/aminoacyl tRNA synthetase specific
513 to L-Anap. The Methyl ester form of L-Anap; L-Anap-Me (AsisChem Inc.) was added to the
514 medium of cells in 35 mm culture dishes from a storing stock solution of 10 mM to a final
515 concentration of 10-20 μM. Through the text, we will refer to L-Anap as Anap for simplicity.
516 Cells were incubated during 12-48 hours before experiments in Dulbecco's Modified Eagle
517 Medium (DMEM, Invitrogen) supplemented with 10% fetal bovine serum (Invitrogen, USA)

518 and penicillin-streptomycin (100 units/ml — 100 μg/ml, Invitrogen, USA) at 37 °C in a 5%
519 CO_2 atmosphere. Around 4 hours before electrophysiological recordings, HEK293 cells
520 were treated with 0.05% trypsin-ethylenediaminetetraacetic acid (Trypsin-EDTA) to
521 obtain rounded cells, which were then re-platted in 35 mm glass-bottom dishes (World
522 Precision Instruments, USA) and used for experiments within 3-6 hrs. All the experiments
523 were performed at room temperature (~25°C).
524
525 *Electrophysiology*
526 Recordings of proton currents were performed in the whole-cell patch-clamp configuration
527 using fire-polished borosilicate micropipettes (Sutter Instruments, USA). Currents were
528 recorded by an Axoclamp 200B amplifier (Axon Instruments, USA) and acquired with an
529 ITC-18 AD/DA converter (HEKA Elektronik, Germany), both controlled with Patchmaster
530 software (HEKA Elektronik, Germany). Currents were low-passed filtered at 5 kHz and
531 sampled at 20 kHz. The extracellular solution contained (in mM): 100
532 tetramethylammonium hydroxide and methanesulfonic acid (TMAOH-$HMESO_3$), 100 buffer
533 ((2-(N-morpholino)ethanesulfonicacid (MES) for pH 5.5, and 6.0; 4-(2-hydroxyethyl)-1-
534 piperazineethanesulfonic acid (HEPES) for pH 7.0 and 7.5), 2 $CaCl_2$, 2 $MgCl_2$, 8 HCl and pH-
535 adjusted with TMAOH and HMESO. The intracellular solution contained (in mM): 80
536 (TMAOH-$HMESO_3$) 100 buffer (MES for pH 5.5 and 6.0; HEPES for pH 7.0 and 7.5), 10
537 ethylene glycol-bis(β-aminoethyl ether)-N,N,N',N'- tetraacetic acid (EGTA), 10 $MgCl_2$, and 4
538 HCl and pH-adjusted with TMAOH and HMESO. With these solutions, patch pipettes had a
539 resistance of 2-5 MΩ. Since cells used in these experiments were round to improve space-
540 clamp and currents were relatively small, no series-resistance compensation was
541 employed. The voltage-clamp protocols varied depending on the value of ΔpH and are
542 indicated in the figure legends. The interval between each test pulse was 45 s at the holding
543 potential to facilitate return of slow fluorescence signals and minimize the effects of proton
544 depletion.
545
546 *Fluorescence measurements*

547 Fluorescence measurements in whole-cell patch-clamp fluorometry (PCF) experiments
548 were made using a TE-2000U (Nikon, Japan) inverted epifluorescence microscope with a
549 60x oil immersion objective (numerical aperture 1.4). A 405 nm solid-state laser (Compass
550 405-50 CW, COHERENT, USA) and a filter cube containing a 405/20-nm excitation filter, a
551 405-nm long pass dichroic mirror, and a 425-nm long-pass emission filter were used for
552 Anap fluorescence excitation. For mCherry fluorescence, measurements were performed
553 using an Ar-Ion laser (Spectra-Physics, Germany) and a filter cube with a 514/10-nm
554 excitation filter, a 514-nm long pass dichroic mirror, and a 530-nm long-pass emission
555 filter (Chroma, USA). Both lasers were through-air coupled, collimated using an optical cage
556 system and appropriate optics (Thorlabs, USA) and then focused into the objective's back
557 focal plane through the microscope's rear port. Imaging was performed using Luca or Ixon
558 Ultra EMCCD cameras (Andor, Oxford instruments, Ireland) controlled by Micromanager
559 software (Edelstein et al., 2014). The fluorescence of a region without cells was measured
560 with the same ROI employed with cells and this background was subtracted from Anap
561 fluorescence images. Image stacks from cells were recorded at 10-25 Hz (100 – 40 ms of
562 exposure, respectively). To improve signal-to-noise ratio, 4x4 or 8x8 pixel binning was
563 used. Initially, fluorescence time course was measured from a region of interest (ROI) that
564 included only the membrane of the patched cell. Identical results were obtained by using a
565 ROI encompassing all the cell.

566 Fluorescence and proton current recording synchronization was achieved through a home-
567 programed Arduino Uno microcontroller board (Arduino, Italy) triggered by a
568 PatchMaster-generated TTL pulse.

569 For spectral measurements, the light from the microscope was collected by a SpectraPro
570 2150i imaging spectrograph (Princeton Instruments, USA) mounted between the
571 microscope and EMCCD camera. The mCherry fluorescence was used as an indicator of
572 membrane-associated channels. A small area from the membrane-associated mCherry
573 fluorescence is selected using the spectrograph slit, and mCherry and Anap spectra were
574 recorded by measuring a line scan 10 pixels wide from the cell membrane spectral image
575 (Figure 2-Supplement 1). Background fluorescence spectrum was recorded from a region

576 of the image without cells and subtracted from Anap and mCherry fluorescence. Unless
577 indicated, all the spectra were obtained at resting potential in non-patched cells (Thomas
578 and Smart, 2005a) and a ΔpH ~ -0.2.
579
580 *Data analysis*
581 IgorPro (Wavemetrics) and ImageJ (NIH) software were used to analyze the data. For the
582 G-V relationships, conductance (G) was calculated from proton currents according to:

$$G(V) = \frac{I(V)}{V - V_{rev}}$$

583 Where V_{rev} is the proton current reversal potential, measured from the current-voltage
584 relation. Then, G was normalized and fit to a Boltzmann function as follows:

$$\frac{G}{G_{max}} = \frac{1}{1 + \exp^{(q(V - V_{0.5})/K_B T)}}$$

585 Equation 1
586 Where q is the apparent gating charge (in elementary charges, e_0), V is the membrane
587 potential, $V_{0.5}$ is the potential at which half of the maximal activation is reached, K_B is the
588 Boltzmann constant and T is the temperature in Kelvin.
589 The time course of fluorescence in PCF experiments, was obtained from all the background-
590 subtracted images in a stack (F_i), and the changes through time were normalized to the first
591 image (F_0) as follows:

$$\frac{F_i - F_0}{F_0} = \frac{\Delta F}{F_0}$$

592 Then, this normalization was multiplied by 100 to obtain the percent change of
593 fluorescence. This procedure was carried out for each stack at each voltage. The voltage-
594 dependence of the fluorescence was estimated from F-V relationships. The value of the
595 fluorescence at the end of the volage step was normalized and fit to a Boltzmann function:

$$\frac{F}{F_{max}} = \frac{1}{1 + \exp^{(q(V - V_{0.5})/K_B T)}}$$

596 Equation 2
597 Where F is the percent of fluorescence change at V potential and F_{max} is the maximum
598 fluorescence percent change in each experiment at V potential. The meaning of q, V, $V_{0.5}$ and

K_BT is the same as in equation 1. All data are presented as the mean ± standard error of the mean (s.e.m.).

The time constants activation of proton currents and fluorescence signals were obtained by fitting of the second half of each trace to the equation:

$$I \text{ or } F(t) = A_{ss}\left(1 - e^{\left(-(t-t_o)/\tau\right)}\right)$$

Equation 3

Where A_{ss} is the amplitude of the fluorescent signal (F) or current (I) at steady state, τ is the time constant, and t_o is the time of start if the voltage pulse, both in ms. The voltage dependence of τ was calculated from a fit to equation:

$$\tau(V) = \tau(0) \cdot e^{\left(\frac{qV}{K_BT}\right)}$$

Equation 4

Where $\tau(0)$ is the activation time constant at 0 mV, q is the partial charge in e_0 units and V, K_B and T have the same meaning as in equation 1.

Modelling

Modelling of current and fluorescence was carried out using custom-written programs in IgorPro (Wavemetrics). The occupancy of each discreet state in the models was calculating by numerically solving the differential equations describing the transitions between states. The occupancy of each discreet state i is P_i and it was calculated by numerically solving the differential equations described by a master equation:

$$\frac{dP_i}{dt} = \sum_{i \neq j}(P_j k_{ji} - P_i k_{ij})$$

The rate constants k_{ij} or k_{ji} are given by:

$$k_{ij} = k_{ij}(0) \cdot \exp\left(-z_{ij}V/K_BT\right)$$

Where $k_{ij}(0)$ is the value of the rate constant at 0 mV, z_{ij} is the partial charge associated with the transition and K_BT have the same meaning as in Eq.1.

The current as a function of time t and voltage V was calculated as:

$$I(t,V) = \gamma_{ch} \cdot N \cdot (V - V_{rev}) \cdot P_o(t,V) + \gamma_{leak} \cdot (V - V_{rev}^{leak})$$

γ_{ch} is the single proton channel conductance, N is the number of channels, V_{rev} is the reversal potential and P_o is the probability of the open state. γ_{leak} is the leak conductance and V_{rev}^{leak} is the reversal potential of the leak currents.

The fluorescence was calculated as:

$$F(t,V) = \sum_{i=0}^{n} P_i\,(t,V) \cdot f_i$$

f_i is the fluorescence of the i-th state in arbitrary units.

Acknowledgements

We thank Eduardo Guevara for measurements of Anap spectra in different solvents and Manuel Hernández for excellent technical support. We thank Dr. Sebastian Brauchi for the loan of the 405 nm laser. This work was supported by DGAPA-PAPIIT-UNAM grant No. IN215621. E. S-D is a doctoral student from Programa de Doctorado en Ciencias Bioquímicas-UNAM and was supported by a doctoral thesis scholarship from CONACyT No. 463819 (CVU 659182). M.E.O-C. is a doctoral student from Programa de Doctorado en Ciencias Biomédicas-UNAM and is supported by a doctoral thesis scholarship from CONACyT No. 788807 (CVU 1101710)

References

Banh, R., V.V. Cherny, D. Morgan, B. Musset, S. Thomas, K. Kulleperuma, S.M.E. Smith, R. Pomès, and T.E. DeCoursey. 2019. Hydrophobic gasket mutation produces gating pore currents in closed human voltage-gated proton channels. *Proc. Natl. Acad. Sci. U.S.A.* 116:18951–18961. doi:10.1073/pnas.1905462116.

Carmona, E.M., M. Fernandez, J.J. Alvear-Arias, A. Neely, H.P. Larsson, O. Alvarez, J.A. Garate, R. Latorre, and C. Gonzalez. 2021. The voltage sensor is responsible for ΔpH dependence in H_v1 channels. *Proc. Natl. Acad. Sci. U.S.A.* 118:e2025556118. doi:10.1073/pnas.2025556118.

Carmona, E.M., H.P. Larsson, A. Neely, O. Alvarez, R. Latorre, and C. Gonzalez. 2018. Gating charge displacement in a monomeric voltage-gated proton (H_v1) channel. *Proc. Natl. Acad. Sci. U.S.A.* 115:9240–9245. doi:10.1073/pnas.1809705115.

655 Catacuzzeno, L., and F. Franciolini. 2022. The 70-year search for the voltage sensing mechanism
656 of ion channels. *The Journal of Physiology*. JP282780. doi:10.1113/JP282780.

657 Cha, A., and F. Bezanilla. 1997. Characterizing Voltage-Dependent Conformational Changes in
658 the K Channel with Fluorescence. *Neuron*. 19:1127–1140. doi:10.1016/S0896-
659 6273(00)80403-1.

660 Cha, A., and F. Bezanilla. 1998. Structural Implications of Fluorescence Quenching in the Shaker
661 K+ Channel. *Journal of General Physiology*. 112:391–408. doi:10.1085/jgp.112.4.391.

662 Chatterjee, A., J. Guo, H.S. Lee, and P.G. Schultz. 2013. A Genetically Encoded Fluorescent Probe
663 in Mammalian Cells. *J. Am. Chem. Soc.* 135:12540–12543. doi:10.1021/ja4059553.

664 Cherny, V.V., V.S. Markin, and T.E. DeCoursey. 1995. The voltage-activated hydrogen ion
665 conductance in rat alveolar epithelial cells is determined by the pH gradient. *The Journal*
666 *of general physiology*. 105:861–896.

667 Cherny, V.V., D. Morgan, B. Musset, G. Chaves, S.M.E. Smith, and T.E. DeCoursey. 2015.
668 Tryptophan 207 is crucial to the unique properties of the human voltage-gated proton
669 channel, hHV1. *Journal of General Physiology*. 146:343–356.
670 doi:10.1085/jgp.201511456.

671 Cowgill, J., and B. Chanda. 2019. The contribution of voltage clamp fluorometry to the
672 understanding of channel and transporter mechanisms. *Journal of General Physiology*.
673 151:1163–1172. doi:10.1085/jgp.201912372.

674 Dai, G., T.K. Aman, F. DiMaio, and W.N. Zagotta. 2019. The HCN channel voltage sensor
675 undergoes a large downward motion during hyperpolarization. *Nat Struct Mol Biol*.
676 26:686–694. doi:10.1038/s41594-019-0259-1.

677 De La Rosa, V., and I.S. Ramsey. 2018. Gating Currents in the Hv1 Proton Channel. *Biophysical*
678 *Journal*. 114:2844–2854. doi:10.1016/j.bpj.2018.04.049.

679 De-la-Rosa, V., E. Suárez-Delgado, G.E. Rangel-Yescas, and L.D. Islas. 2016. Currents through
680 Hv1 channels deplete protons in their vicinity. *Journal of General Physiology*. 147:127–
681 136. doi:10.1085/jgp.201511496.

682 Eckert, R., and T. Sibaoka. 1968. The Flash-Triggering Action Potential of the Luminescent
683 Dinoflagellate Noctiluca. *Journal of General Physiology*. 52:258–282.
684 doi:10.1085/jgp.52.2.258.

685 Edelstein, A.D., M.A. Tsuchida, N. Amodaj, H. Pinkard, R.D. Vale, and N. Stuurman. 2014.
686 Advanced methods of microscope control using μManager software. *J Biol Methods*.
687 1:e10. doi:10.14440/jbm.2014.36.

688 Gonzalez, C., G.F. Contreras, A. Peyser, P. Larsson, A. Neely, and R. Latorre. 2012. Voltage
689 sensor of ion channels and enzymes. *Biophys Rev*. 4:1–15. doi:10.1007/s12551-011-
690 0061-8.

691 Gordon, S.E., M. Munari, and W.N. Zagotta. 2018. Visualizing conformational dynamics of
692 proteins in solution and at the cell membrane. *eLife*. 7:e37248. doi:10.7554/eLife.37248.

693 Hondares, E., M.A. Brown, B. Musset, D. Morgan, V.V. Cherny, C. Taubert, M.K. Bhamrah, D.
694 Coe, F. Marelli-Berg, J.G. Gribben, M.J.S. Dyer, T.E. DeCoursey, and M. Capasso. 2014.
695 Enhanced activation of an amino-terminally truncated isoform of the voltage-gated
696 proton channel HVCN1 enriched in malignant B cells. *Proc. Natl. Acad. Sci. U.S.A.*
697 111:18078–18083. doi:10.1073/pnas.1411390111.

698 Hong, L., M.M. Pathak, I.H. Kim, D. Ta, and F. Tombola. 2013. Voltage-sensing domain of
699 voltage-gated proton channel Hv1 shares mechanism of block with pore domains.
700 *Neuron*. 77:274–287.

701 Islas, L.D., and W.N. Zagotta. 2006. Short-range Molecular Rearrangements in Ion Channels
702 Detected by Tryptophan Quenching of Bimane Fluorescence. *Journal of General*
703 *Physiology*. 128:337–346. doi:10.1085/jgp.200609556.

704 Kalstrup, T., and R. Blunck. 2013. Dynamics of internal pore opening in K_V channels probed by a
705 fluorescent unnatural amino acid. *Proc. Natl. Acad. Sci. U.S.A.* 110:8272–8277.
706 doi:10.1073/pnas.1220398110.

707 Kalstrup, T., and R. Blunck. 2018. S4–S5 linker movement during activation and inactivation in
708 voltage-gated K^+ channels. *Proc. Natl. Acad. Sci. U.S.A.* 115.
709 doi:10.1073/pnas.1719105115.

710 Klymchenko, A.S. 2017. Solvatochromic and Fluorogenic Dyes as Environment-Sensitive Probes:
711 Design and Biological Applications. *Acc. Chem. Res.* 50:366–375.
712 doi:10.1021/acs.accounts.6b00517.

713 Koch, H.P., T. Kurokawa, Y. Okochi, M. Sasaki, Y. Okamura, and H.P. Larsson. 2008. Multimeric
714 nature of voltage-gated proton channels. *Proc. Natl. Acad. Sci. U.S.A.* 105:9111–9116.
715 doi:10.1073/pnas.0801553105.

716 Kusch, J., and G. Zifarelli. 2014a. Patch-Clamp Fluorometry: Electrophysiology meets
717 Fluorescence. *Biophysical Journal*. 106:1250–1257. doi:10.1016/j.bpj.2014.02.006.

718 Kusch, J., and G. Zifarelli. 2014b. Patch-Clamp Fluorometry: Electrophysiology meets
719 Fluorescence. *Biophysical Journal*. 106:1250–1257. doi:10.1016/j.bpj.2014.02.006.

720 Lee, S.-Y., J.A. Letts, and R. MacKinnon. 2008. Dimeric subunit stoichiometry of the human
721 voltage-dependent proton channel Hv1. *Proc. Natl. Acad. Sci. U.S.A.* 105:7692–7695.
722 doi:10.1073/pnas.0803277105.

723 Li, Q., R. Shen, J.S. Treger, S.S. Wanderling, W. Milewski, K. Siwowska, F. Bezanilla, and E.
724 Perozo. 2015. Resting state of the human proton channel dimer in a lipid bilayer. *Proc.*
725 *Natl. Acad. Sci. U.S.A.* 112. doi:10.1073/pnas.1515043112.

726 Lishko, P.V., and Y. Kirichok. 2010. The role of Hv1 and CatSper channels in sperm activation:
727 Hv1 and CatSper channels in sperm activation. *The Journal of Physiology*. 588:4667–
728 4672. doi:10.1113/jphysiol.2010.194142.

729 Ma, J., X. Gao, Y. Li, T.E. DeCoursey, G.E. Shull, and H. Wang. 2022. The HVCN1 voltage-gated
730 proton channel contributes to pH regulation in canine ventricular myocytes. *The Journal*
731 *of Physiology*. 600:2089–2103. doi:10.1113/JP282126.

732 Mizutani, N., A. Kawanabe, Y. Jinno, H. Narita, T. Yonezawa, A. Nakagawa, and Y. Okamura.
733 2022. Interaction between S4 and the phosphatase domain mediates electrochemical
734 coupling in voltage-sensing phosphatase (VSP). *Proc. Natl. Acad. Sci. U.S.A.*
735 119:e2200364119. doi:10.1073/pnas.2200364119.

736 Mony, L., T.K. Berger, and E.Y. Isacoff. 2015. A specialized molecular motion opens the Hv1
737 voltage-gated proton channel. *Nat Struct Mol Biol*. 22:283–290. doi:10.1038/nsmb.2978.

738 Munteanu, B., M. Braun, and K. Boonrod. 2012. Improvement of PCR reaction conditions for
739 site-directed mutagenesis of big plasmids. *J. Zhejiang Univ. Sci. B*. 13:244–247.
740 doi:10.1631/jzus.B1100180.

741 Musset, B., V.V. Cherny, D. Morgan, Y. Okamura, I.S. Ramsey, D.E. Clapham, and T.E. DeCoursey.
742 2008. Detailed comparison of expressed and native voltage-gated proton channel
743 currents: Voltage-dependent proton channel gating. *The Journal of Physiology*.
744 586:2477–2486. doi:10.1113/jphysiol.2007.149427.

745 Pantazis, A., and R. Olcese. 2012. Relative transmembrane segment rearrangements during BK
746 channel activation resolved by structurally assigned fluorophore–quencher pairing.
747 *Journal of General Physiology*. 140:207–218. doi:10.1085/jgp.201210807.

748 Puljung, M.C. 2021. ANAP: A versatile, fluorescent probe of ion channel gating and regulation.
749 *In* Methods in Enzymology. Elsevier. 49–84.

750 Qiu, F., S. Rebolledo, C. Gonzalez, and H.P. Larsson. 2013. Subunit Interactions during
751 Cooperative Opening of Voltage-Gated Proton Channels. *Neuron*. 77:288–298.
752 doi:10.1016/j.neuron.2012.12.021.

753 Ramsey, I.S., Y. Mokrab, I. Carvacho, Z.A. Sands, M.S.P. Sansom, and D.E. Clapham. 2010. An
754 aqueous H+ permeation pathway in the voltage-gated proton channel Hv1. *Nat Struct*
755 *Mol Biol*. 17:869–875. doi:10.1038/nsmb.1826.

Ramsey, I.S., M.M. Moran, J.A. Chong, and D.E. Clapham. 2006. A voltage-gated proton-selective channel lacking the pore domain. *Nature*. 440:1213–1216. doi:10.1038/nature04700.

Ramsey, I.S., E. Ruchti, J.S. Kaczmarek, and D.E. Clapham. 2009. Hv1 proton channels are required for high-level NADPH oxidase-dependent superoxide production during the phagocyte respiratory burst. *Proc. Natl. Acad. Sci. U.S.A.* 106:7642–7647. doi:10.1073/pnas.0902761106.

Randolph, A.L., Y. Mokrab, A.L. Bennett, M.S. Sansom, and I.S. Ramsey. 2016. Proton currents constrain structural models of voltage sensor activation. *eLife*. 5:e18017. doi:10.7554/eLife.18017.

Rangel-Yescas, G., C. Cervantes, M.A. Cervantes-Rocha, E. Suárez-Delgado, A.T. Banaszak, E. Maldonado, I.S. Ramsey, T. Rosenbaum, and L.D. Islas. 2021. Discovery and characterization of Hv1-type proton channels in reef-building corals. *eLife*. 10:e69248. doi:10.7554/eLife.69248.

Sasaki, M., M. Takagi, and Y. Okamura. 2006. A Voltage Sensor-Domain Protein Is a Voltage-Gated Proton Channel. *Science*. 312:589–592. doi:10.1126/science.1122352.

Schladt, T.M., and T.K. Berger. 2020. Voltage and pH difference across the membrane control the S4 voltage-sensor motion of the Hv1 proton channel. *Sci Rep*. 10:21293. doi:10.1038/s41598-020-77986-z.

Shaner, N.C., R.E. Campbell, P.A. Steinbach, B.N.G. Giepmans, A.E. Palmer, and R.Y. Tsien. 2004. Improved monomeric red, orange and yellow fluorescent proteins derived from Discosoma sp. red fluorescent protein. *Nat Biotechnol*. 22:1567–1572. doi:10.1038/nbt1037.

Smith, S.M.E., D. Morgan, B. Musset, V.V. Cherny, A.R. Place, J.W. Hastings, and T.E. DeCoursey. 2011. Voltage-gated proton channel in a dinoflagellate. *Proc. Natl. Acad. Sci. U.S.A.* 108:18162–18167. doi:10.1073/pnas.1115405108.

Stefani, E., M. Ottolia, F. Noceti, R. Olcese, M. Wallner, R. Latorre, and L. Toro. 1997. Voltage-controlled gating in a large conductance Ca^{2+}-sensitive K^{+} channel (hslo). *Proc. Natl. Acad. Sci. U.S.A.* 94:5427–5431. doi:10.1073/pnas.94.10.5427.

Tao, X., A. Lee, W. Limapichat, D.A. Dougherty, and R. MacKinnon. 2010. A Gating Charge Transfer Center in Voltage Sensors. *Science*. 328:67–73. doi:10.1126/science.1185954.

Taylor, A.R., A. Chrachri, G. Wheeler, H. Goddard, and C. Brownlee. 2011. A Voltage-Gated H+ Channel Underlying pH Homeostasis in Calcifying Coccolithophores. *PLoS Biol*. 9:e1001085. doi:10.1371/journal.pbio.1001085.

790 Thomas, P., and T.G. Smart. 2005a. HEK293 cell line: A vehicle for the expression of
791 recombinant proteins. *Journal of Pharmacological and Toxicological Methods*. 51:187–
792 200. doi:10.1016/j.vascn.2004.08.014.

793 Thomas, P., and T.G. Smart. 2005b. HEK293 cell line: A vehicle for the expression of
794 recombinant proteins. *Journal of Pharmacological and Toxicological Methods*. 51:187–
795 200. doi:10.1016/j.vascn.2004.08.014.

796 Tombola, F., M.H. Ulbrich, and E.Y. Isacoff. 2008. The Voltage-Gated Proton Channel Hv1 Has
797 Two Pores, Each Controlled by One Voltage Sensor. *Neuron*. 58:546–556.
798 doi:10.1016/j.neuron.2008.03.026.

799 Vaid, M., T.W. Claydon, S. Rezazadeh, and D. Fedida. 2008. Voltage Clamp Fluorimetry Reveals a
800 Novel Outer Pore Instability in a Mammalian Voltage-gated Potassium Channel. *Journal*
801 *of General Physiology*. 132:209–222. doi:10.1085/jgp.200809978.

802 Villalba-Galea, C.A. 2014. Hv1 proton channel opening is preceded by a voltage-independent
803 transition. *Biophysical journal*. 107:1564–1572.

804 Wang, Y., S.J. Li, X. Wu, Y. Che, and Q. Li. 2012. Clinicopathological and Biological Significance of
805 Human Voltage-gated Proton Channel Hv1 Protein Overexpression in Breast Cancer.
806 *Journal of Biological Chemistry*. 287:13877–13888. doi:10.1074/jbc.M112.345280.

807 Wu, L.-J. 2014. Microglial Voltage-Gated Proton Channel Hv1 in Ischemic Stroke. *Transl. Stroke*
808 *Res.* 5:99–108. doi:10.1007/s12975-013-0289-7.

809 Wu, X., L. Zhang, and L. Hong. 2022. The role of Phe150 in human voltage-gated proton
810 channel. *iScience*. 25:105420. doi:10.1016/j.isci.2022.105420.

811 Young, V.C., and P. Artigas. 2021. Displacement of the Na^+/K^+ pump's transmembrane
812 domains demonstrates conserved conformational changes in P-type 2 ATPases. *Proc.*
813 *Natl. Acad. Sci. U.S.A.* 118:e2019317118. doi:10.1073/pnas.2019317118.

814 Yu, Y., X. Luo, C. Li, F. Ding, M. Wang, M. Xie, Z. Yu, B.R. Ransom, and W. Wang. 2020. Microglial
815 Hv1 proton channels promote white matter injuries after chronic hypoperfusion in mice.
816 *J. Neurochem.* 152:350–367. doi:10.1111/jnc.14925.

817 Zhang, L., K. Bellve, K. Fogarty, and W.R. Kobertz. 2016. Fluorescent Visualization of Cellular
818 Proton Fluxes. *Cell Chemical Biology*. 23:1449–1457.
819 doi:10.1016/j.chembiol.2016.10.013.

820 Zhang, Q., Y. Ren, Y. Mo, P. Guo, P. Liao, Y. Luo, J. Mu, Z. Chen, Y. Zhang, Y. Li, L. Yang, D. Liao, J.
821 Fu, J. Shen, W. Huang, X. Xu, Y. Guo, L. Mei, Y. Zuo, J. Liu, H. Yang, and R. Jiang. 2022.
822 Inhibiting Hv1 channel in peripheral sensory neurons attenuates chronic inflammatory
823 pain and opioid side effects. *Cell Res*. 32:461–476. doi:10.1038/s41422-022-00616-y.

824 Zhao, C., and F. Tombola. 2021. Voltage-gated proton channels from fungi highlight role of
825 peripheral regions in channel activation. *Commun Biol*. 4:261. doi:10.1038/s42003-021-
826 01792-0.

827 Zhao, R., K. Kennedy, G.A. De Blas, G. Orta, M.A. Pavarotti, R.J. Arias, J.L. de la Vega-Beltrán, Q.
828 Li, H. Dai, E. Perozo, L.S. Mayorga, A. Darszon, and S.A.N. Goldstein. 2018. Role of
829 human Hv1 channels in sperm capacitation and white blood cell respiratory burst
830 established by a designed peptide inhibitor. *Proc. Natl. Acad. Sci. U.S.A.* 115.
831 doi:10.1073/pnas.1816189115.

832 Zheng, L., U. Baumann, and J.-L. Reymond. 2004. An efficient one-step site-directed and site-
833 saturation mutagenesis protocol. *Nucleic Acids Research*. 32:e115.
834 doi:10.1093/nar/gnh110.

835

836

837 **Figure legends**

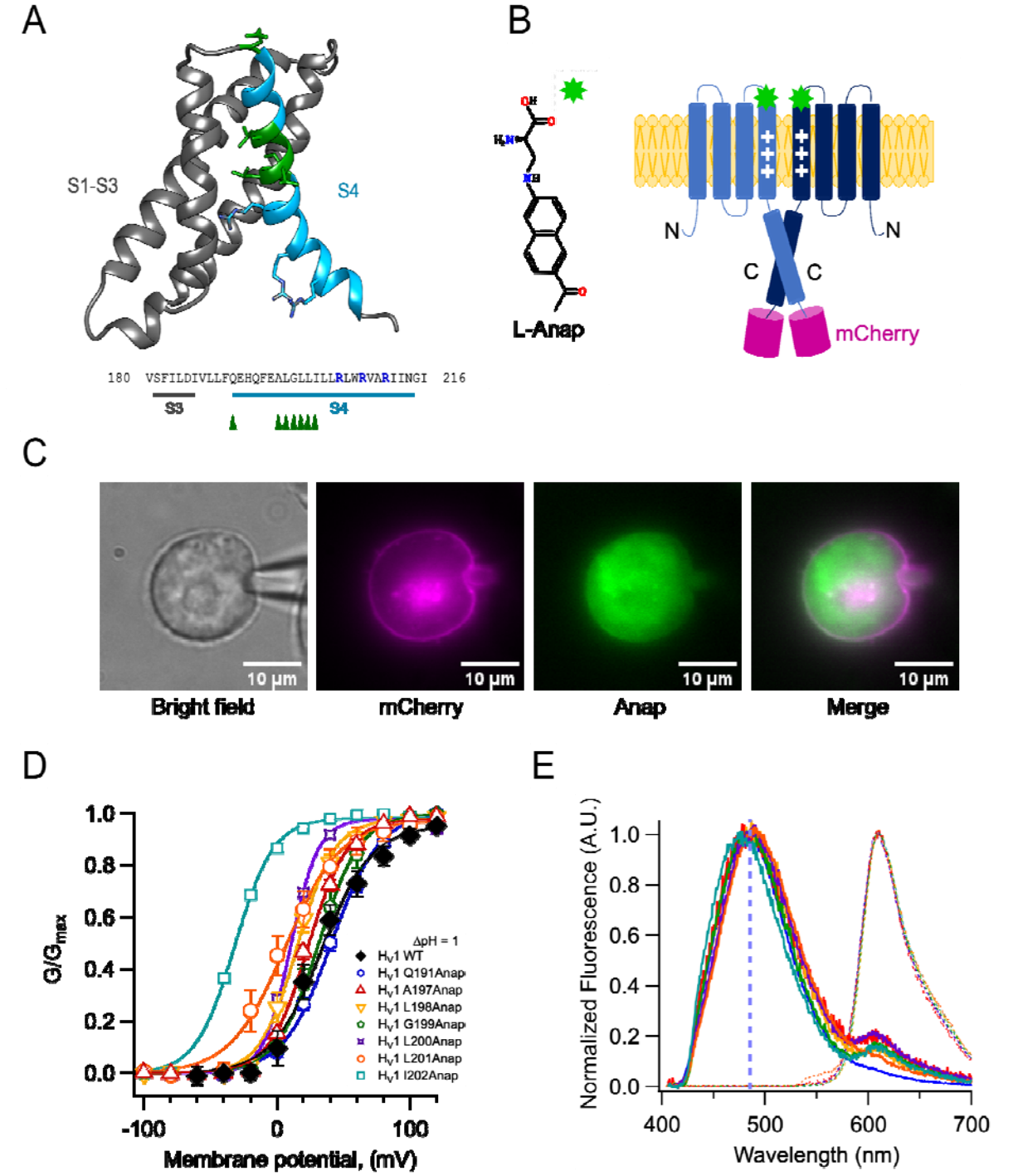

838 Figure 1

839 **Figure 1.** Anap as a fluorescent probe in hH_V1. A) Ribbon representation of
840 transmembrane segments S1-S4 of closed hH_V1 based on the model of Randolph et al.
841 (Randolph et al., 2016). S1-S3 are in grey whereas S4 is in light blue. S4 positively charged
842 arginine residues are shown as cyan sticks, whereas the residues where Anap was
843 incorporated individually in the S4 segment are depicted as green sticks and with green
844 arrow heads in the S3-S4 sequence below; positively charged arginine residues are
845 indicated in marine blue. B) Structure of non-canonical amino acid Anap (left), and a
846 schematic representation (right) that shows the incorporation of Anap (green star) into the
847 hH_V1 dimer expressed in HEK293 cells. An mCherry fluorescent protein (magenta cylinder)
848 was fused to the C-terminal end of hH_V1 as an Anap incorporation reporter. C) Images of a
849 representative Patch-clamp Fluorometry (PCF) experiment, showing the voltage-clamped
850 cell and the co-localization of Anap and mCherry fluorescence in the cell membrane for
851 Anap incorporated at position Q191 of hH_V1. D) G-V curves obtained from currents
852 produced by each hH_V1 mutant rescued by Anap incorporation. All G-V s were obtained at
853 ΔpH=1 and compared with hH_V1 WT. Continuous lines are the fit of the conductance data to
854 equation 1; fit parameters are summarized in Supplemental table I. The incorporation of
855 Anap at the I202 site sifts the G-V ~65 mV to more negative potentials. Data shown are
856 mean ± s.e.m. E) Normalized mean emission spectrum of Anap (continuous lines) and
857 mCherry (dashed lines) at each incorporation site (color code from D) recorded at resting
858 potential in non-patched cells. Q191(n=15); A197(n=8); L198(n=7); G199(n=6);
859 L200(n=10); L201(n=30); I202(n=10). The vertical blue line indicates the peak emission of
860 Anap in water (486 nm). A second emission peak can be distinguished in every position
861 inside S4 where Anap was incorporated, except Q191Anap. This peak is located around 610
862 nm which coincides with the peak emission of mCherry.
863

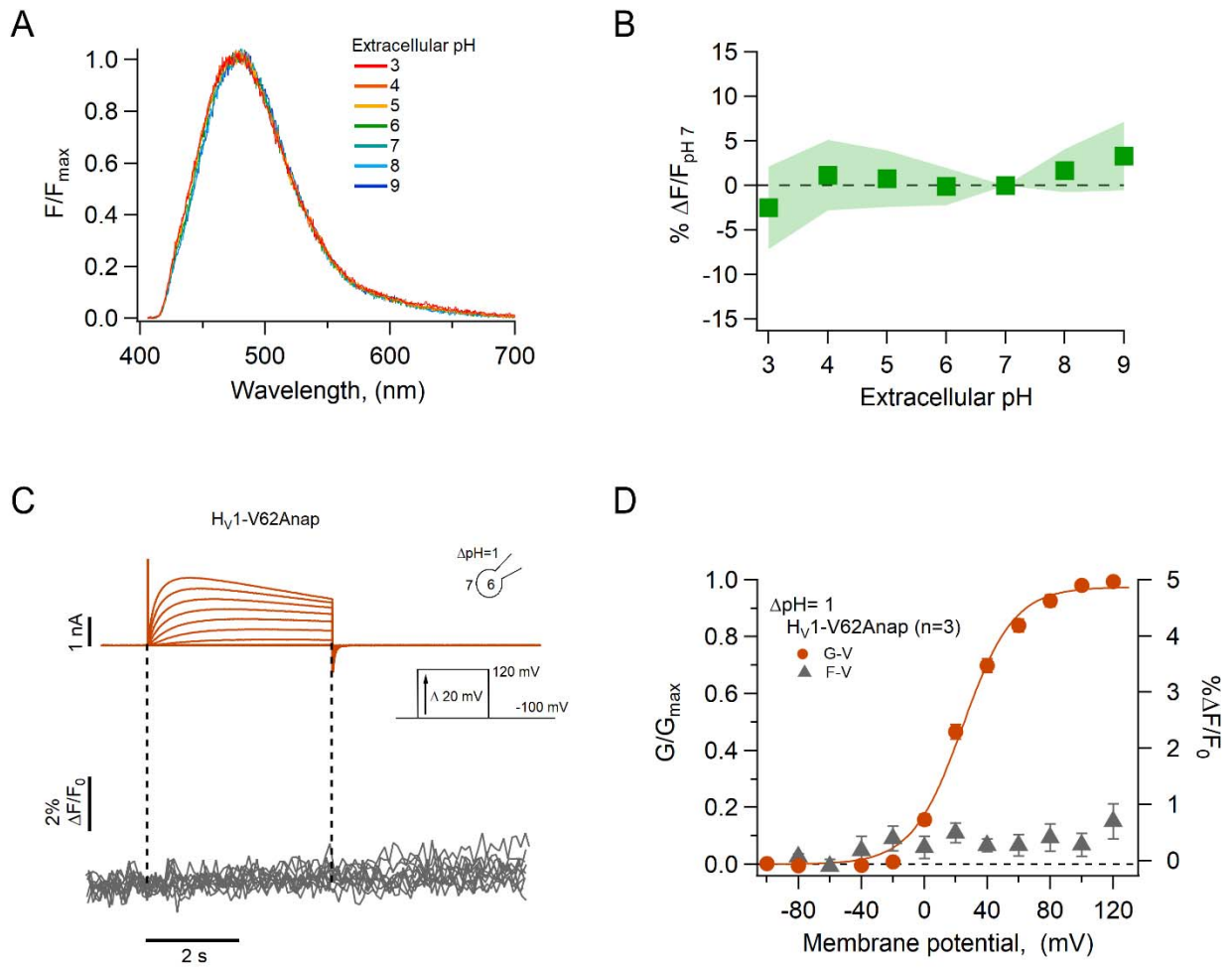

Figure 2

Figure 2. The fluorescence of incorporated Anap is stable to external acidity and local pH changes. A) Mean spectra of Anap fluorescence in the hH_V1-Q191Anap mutant at each external pH tested (pH_o) recorded at the resting potential in non-patched cells. The emission peak of spectra of Anap remained inside the wavelength range of 475-480 nm. B) Percentage of fluorescence intensity change normalized to fluorescence at pH_o 7 in hH_V1-Q191Anap mutant (n=13). The intensity was measured from the peak of emission spectra. C) Representative PCF experiments with the hH_V1-V62Anap mutant. Currents (upper panel, orange traces) and fluorescent signal (lower panel, gray traces) were elicited in response to voltage pulses from -100 mV to 120 mV in steps of 20 mV. D) F-V and G-V relationships from the experiments shown in C. Relative fluorescence changes at the end of voltage test pulses are shown in gray triangles, and conductance is shown in orange circles.

The orange continuous line is the fit to equation 1 of G-V data (fit parameters: $V_{0.5}$ = 24.4 ± 1.6 mV; q = 1.5 ± 0.1 e_0). Data in B and D are Mean ± s.e.m.

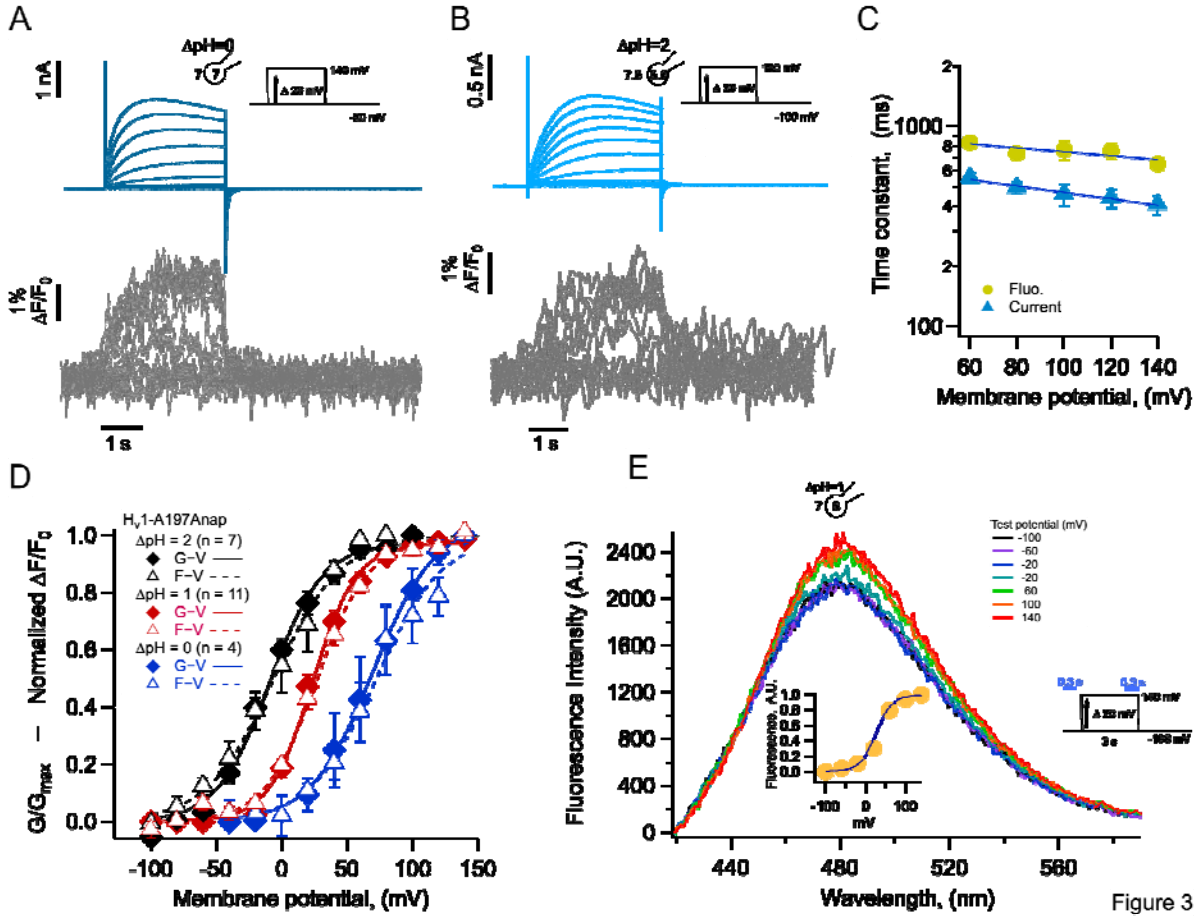

Figure 3

Figure 3. Anap incorporation in position A197 reveals that the movement of S4 is modulated by ΔpH. A-B) Representative PCF experiment with A197Anap at ΔpH=0 and ΔpH=2, respectively. Proton current families (upper panels) are shown in blue traces and fluorescent Anap signal (lower panel) in gray traces. C) Activation time constant of current (blue) and fluorescent (lemon) signals at ΔpH=0 obtained by fitting Eq. 3. The dark blue curve shows the exponential fit to Eq. 4. The fit parameters were: $\tau(0)$ = 935 ms and q = -0.06 e_0 for fluorescence and 678 ms and -0.09 e_0 for current. D) F-V (empty triangles) and G-V (filled diamonds) curves and different ΔpH values (ΔpH=0 in blue; ΔpH=1 in red; ΔpH=2 in black). The data were fit to equation 1(G-V, continuous curves; F-V, discontinuous curves) with the following parameters: ΔpH=0; F-V: $V_{0.5}$ = 72.3 ± 6 mV; q = 1.0 ± 0.1 e_0. G-V: $V_{0.5}$ = 69.6 ± 1.5 mV; q = 1.1 ± 0.1 e_0. ΔpH =1; F-V: $V_{0.5}$ = 26.6 ± 1.5 mV; q = 1.3± 0.1 e_0. G-V: $V_{0.5}$ = 23.4 ± 1.3 mV; q = 1.5 ± 0.1 e_0. ΔpH = 2; F-V: $V_{0.5}$ = -6.1 ± 1.8 mV; q = 1.0 ± 0.1 e_0. G-V:

894 $V_{0.5}$ = -9.2 ± 2.3 mV; q = 1.2 ± 2.4 e_0. E) Emission spectra of Anap in the A197Anap mutant
895 obtained in steady-state (300 ms at the end of holding potential and the end of the test
896 pulse, green bars in the inset) in response to different voltages (color code indicates the
897 test pulse in mV: purple, -60; dark blue, -40; light blue, 20; cyan, 0; light green, 20; dark
898 green, 40; olive, 60; yellow, 80; orange, 100; dark red, 120; red, 140). The inset plots the
899 amplitude of the emission peak as a function of test voltage. The smooth curve is the fit of
900 the fluorescence data at ΔpH=1 shown in panel D. Summary data shown in C and D are
901 mean ± s.e.m.
902
903

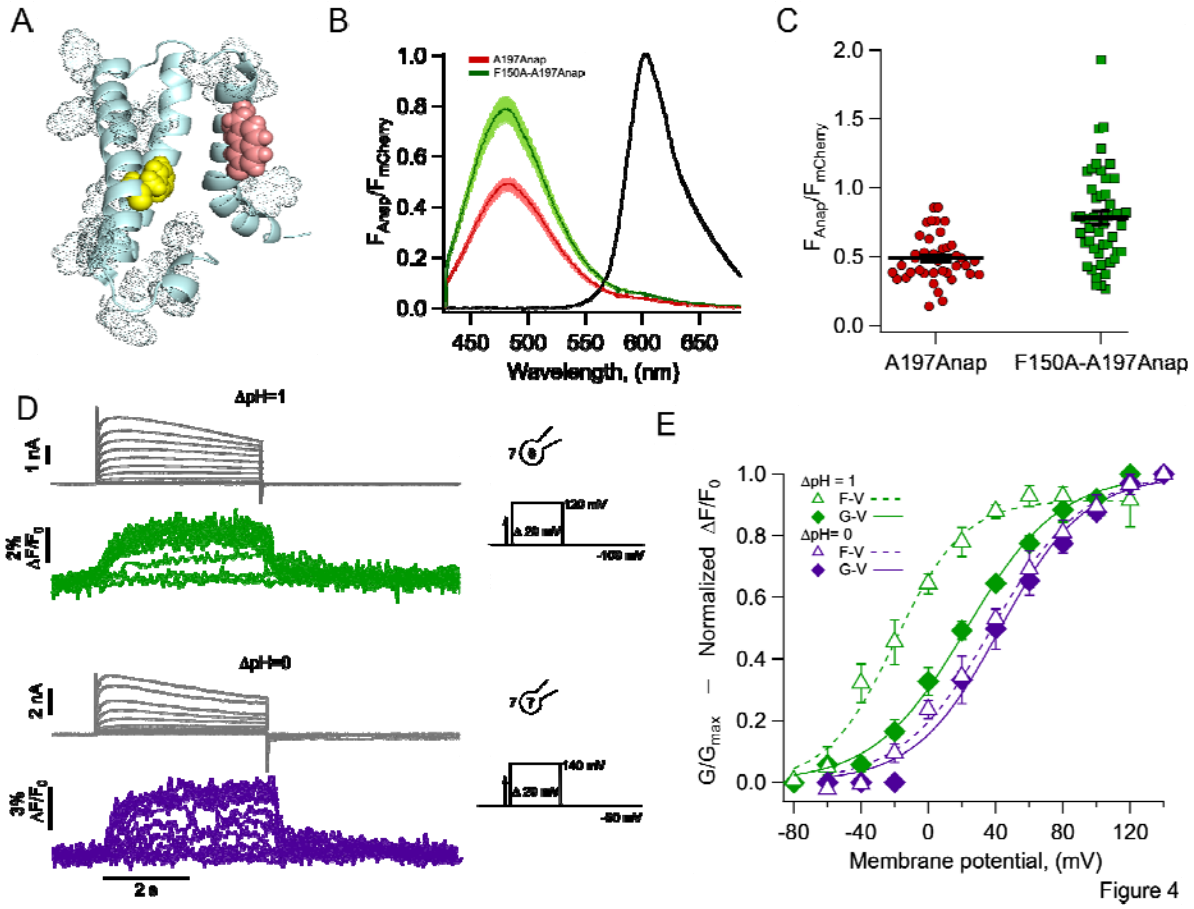

Figure 4. The charge transfer center (F150) is an Anap quencher. A) Cartoon showing the presence of aromatic residues in hH_V1 (rendered as space-filling dots, main chain in light blue, S3 was removed for illustration). F150 in yellow and Anap in pink. B) Averages of spectra of Anap incorporated in both mutants (H_V1-A197Anap, red; H_V1-F150A-A197Anap, green) normalized to the fluorescence of mCherry (black). Spectra were obtained at the resting potential in non-patched cells. The double mutant's brightness is approximately 60% higher. Shadows represent s.e.m. C) Comparison of the intensity of the emission spectrum peak of Anap normalized to the intensity of the fluorescent protein mCherry between the mutant H_V1-A197Anap-Cherry (0.49 ± 0.03) and double mutant H_V1-F150A-A197Anap-Cherry (0.79 ± 0.05), taken at 48 hours post-transfection. Each point indicates an individual spectrum measured from a single cell; n = 41 and 49, respectively. Black

horizontal lines are the mean ± s.e.m. T-test value $p < 0.001$. D) Representative current and fluorescence traces from PCF experiments of the double mutant H_V1-F150A-A197Anap at ΔpH=1 (upper panel) and ΔpH=0 (lower panel). E) Comparison of G-V (diamonds) and F-V (triangles) relationship between both ΔpH conditions (ΔpH=1 in green; ΔpH=0 in purple) of the double mutant H_V1-F150A-A197Anap. F-V curve of H_V1-F150A-A197Anap at ΔpH=0 is shifted negatively around 58 mV compared to ΔpH=1. Boltzmann fit parameters of H_V1-F150A-A197Anap were: ΔpH=1 F-V: $V_{0.5}$=-19.8 ± 2.7 mV; q =1.2 ± 0.1 e_0; G-V: $V_{0.5}$ = 22.7 ± 2.3 mV; q = 0.9 ± 0.1 e_0. ΔpH=0 F-V: $V_{0.5}$=38.0 ± 3.0 mV; q =0.9 ± 0.1 e_0; G-V: $V_{0.5}$ = 42.6 ± 3.8 mV; q = 1.0 ± 0.1 e_0. Data shown in B, C and E are mean ± s.e.m.

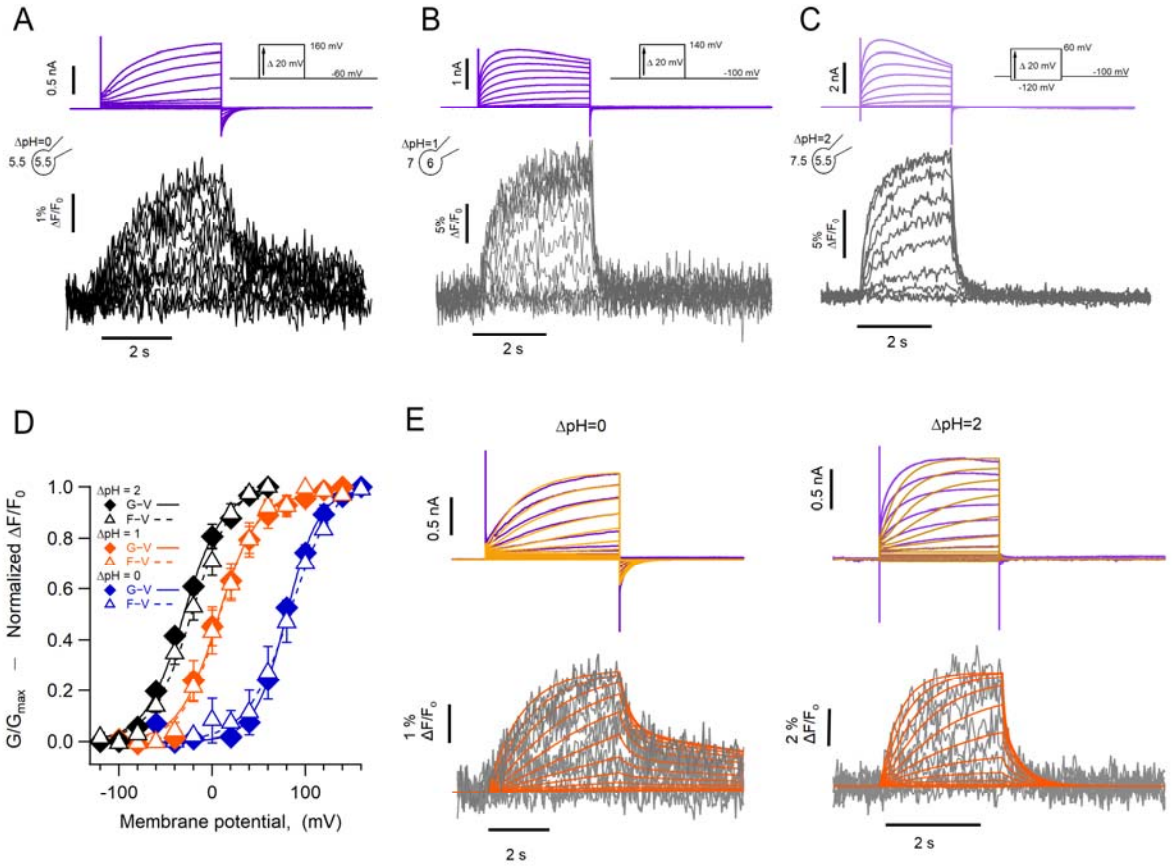

Figure 5

Figure 5. The kinetics of fluorescent signal during deactivation is strongly modulated by pH. Representative PCF experiments with the hH_V1-L201Anap mutant at: A) ΔpH=0. B) ΔpH=1. C) ΔpH=2. Current families are shown in the upper panel (purple traces) and fluorescent signals in the lower panel (black and gray traces). D) G-V (filled diamonds) and F-V (empty triangles) relationships at ΔpH=0 (blue markers, n = 3), ΔpH=1 (orange markers, n=4) and ΔpH=2 (black markers, n=5) of mutant hH_V1-L201Anap. Data are mean ± s.e.m. Note that the difference between the activation at ΔpH=1 and ΔpH=0 is around 77 mV/ΔpH unit. Boltzmann fit parameters: ΔpH=0, F-V; $V_{0.5}$= 84.6 ± 2.1 mV, q =1.0 e_0 ± 0.1. G-V; $V_{0.5}$= 79.7 ± 1.8 mV, q = 1.4 ± 0.1 e_0. ΔpH =1, F-V; $V_{0.5}$= 7.7 ± 1.6 mV, q =1.2 ± 0.1 e_0. G-V: $V_{0.5}$= 6.3 ± 2.2 mV; q = 1.2 ± 0.1 e_0. ΔpH = 2, F-V: $V_{0.5}$= -21.1 ± 2.3 mV; q =1.1 ± 0.1 e_0. G-V: $V_{0.5}$= -30.7 ± 1.9 mV; q = 1.2 ± 0.1 e_0. E) Comparison of the current and fluorescence at two values of ΔpH with the predictions of the sequential activation model in Scheme I.

Experimental current and fluorescence traces are color coded as in A). Simulated current traces are mustard colored and fluorescence traces are orange. Simulation parameters can be found in Supplementary Table II.

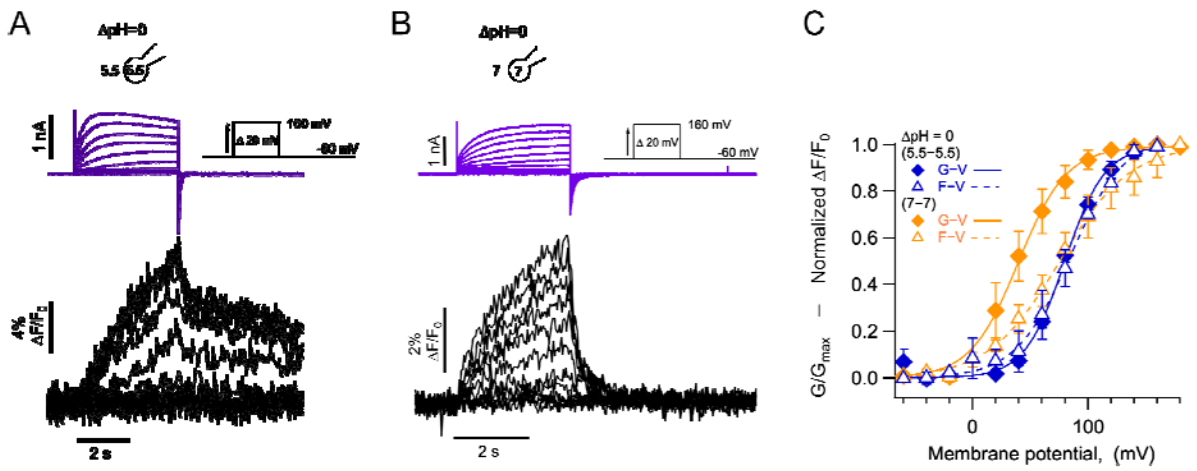

Figure 6

Figure 6. Absolute pH values are gating determinants in hH_V1-L201Anap. A) Representative PCF experiment at ΔpH=0 (5.5_o-5.5_i). Currents are purple and fluorescence black. B) Similar experiment to A) with ΔpH=0 (7_o-7_i). Current and fluorescence traces color coded as in A). C) G-V (filled diamonds) and F-V (empty triangles) curves at ΔpH=0 but with different absolute pH values (pH_o/pH_i =5.5/5.5 in blue; pH_o/pH_i =7/7 in orange, n= 4). Boltzmann fit parameters were pH_o/pH_i =7/7 F-V: $V_{0.5}$= 75.3 ± 2.2 mV; q =0.8 ± 0.04 e_0. G-V: $V_{0.5}$= 39.6 ± 1.3 mV; q = 1.2 ± 0.1 e_0. pH_o/pH_i =5.5/5.5 F-V: $V_{0.5}$= 84.6 ± 2.1 mV; q =1.0 e_0 ± 0.1. G-V: $V_{0.5}$= 79.7 ± 1.8 mV; q = 1.4 ± 0.1 e_0. Data are mean ± s.e.m.